dissolved methane in sea water[27]. Briefly, sea water was transferred directly from the serum vial to a sparging column, and the dissolved gases stripped with ultra-pure He for 12 min. Air samples were flushed into the sparger by introduction into the carrier stream via the standard loop upstream of the sparger. The sparged gases were passed through columns containing Drierite and Ascarite to remove excess water vapour and CO_2, respectively, and the remaining condensable gases were trapped in a stainless-steel column immersed in liquid nitrogen. These gases were cryofocused[28], before separating N_2O from CO_2 and other trapped gases using a PoraPLOT-Q (25 m × 0.32 mm) analytical column held at 10 °C. N_2O was then introduced directly into the ion source of a MAT 252 isotope-ratio-monitoring gas chromatograph/mass spectrometer (irmGC/MS). N_2O concentration and stable-isotope ratios ($^{15}R = {}^{15}N/{}^{14}N$ and $^{18}R = {}^{18}O/{}^{16}O$) were measured simultaneously by monitoring the ion currents of masses 44, 45 and 46 using the Finnigan ISODAT software. Nitrogen-isotope enrichments were corrected for the contribution of ^{17}O to the mass 45 ion current[29,30]. We report all isotopic values as per mil deviations with respect to atmospheric N_2 and O_2 using standard delta notation: $\delta(‰) = [(R_{sample}/R_{standard}) - 1] \times 1{,}000$. Our analytical scheme is capable of analysing as little as 1 nanomole of N_2O in less than 45 min. Analyses of samples in duplicate or triplicate yield reproducibilities of approximately ±0.3‰ for $\delta^{15}N$ and ±0.7‰ for $\delta^{18}O$ of dissolved N_2O in near-surface waters. We characterized the isotopic composition of our standard gas with respect to internationally accepted standards by the conversion of N_2O to N_2 plus CO_2 (refs 6, 31), followed by cryogenic separation and analysis of the gases produced using traditional methods. Calibration of N_2O concentration was achieved using a commercial gas mixture, and double-checked using dilutions of high-purity N_2O in He.

Received 31 December 1997; accepted 21 August 1998.

1. Houghton, J. T., Jenkins, G. J. & Ephraums, J. J. (eds) *Climate Change: The IPCC Scientific Assessment* (Cambridge Univ. Press, 1990).
2. Crutzen, P. J. The influence of nitrogen oxides on the atmospheric ozone content. *Q. J. R. Meteorol. Soc.* **96,** 320–325 (1970).
3. Bouwman, A. F., Van der Hoek, K. W. & Olivier, J. G. J. Uncertainties in the global source distribution of nitrous oxide. *J. Geophys. Res.* **100,** 2785–2800 (1995).
4. Kim, K.-R. & Craig, H. Nitrogen-15 and oxygen-18 characteristics of nitrous oxide: a global perspective. *Science* **262,** 1855–1857 (1993).
5. McElroy, M. B. & Jones, D. B. A. Evidence for an additional source of atmospheric N_2O. *Glob. Biogeochem. Cycles* **10,** 651–659 (1996).
6. Kim, K.-R. & Craig, H. Two-isotope characterization of N_2O in the Pacific Ocean and constraints on its origin in deep water. *Nature* **347,** 58–61 (1990).
7. Zafiriou, O. Laughing gas from leaky pipes. *Nature* **347,** 15–16 (1990).
8. Karl, D. M. & Lukas, R. The Hawaii Ocean Time-series (HOT) program: background, rationale and field implementation. *Deep-Sea Res. II* **43,** 129–156 (1996).
9. Alldredge, A. L. & Cohen, Y. Can microscale chemical patches persist in the sea? Microelectrode study of marine snow, fecal pellets. *Science* **235,** 689–691 (1987).
10. Yoshida, N., Hattori, A., Saino, T., Matsuo, S. & Wada, E. $^{15}N/^{14}N$ ratio of dissolved N_2O in the eastern tropical Pacific Ocean. *Nature* **307,** 442–444 (1984).
11. Yamazaki, T., Yoshida, N., Wada, E. & Matsuo, S. N_2O reduction by *Azotobacter vinelandii* with emphasis on kinetic isotope effects. *Plant Cell Physiol.* **28,** 263–271 (1989).
12. Ward, B. B. in *Nitrification* (ed. Prosser, J. I.) 157–184 (IRL, Oxford, 1986).
13. Dore, J. E. & Karl, D. M. Nitrification in the euphotic zone as a source for nitrite, nitrate and nitrous oxide at Station ALOHA. *Limnol. Oceanogr.* **41,** 1619–1628 (1996).
14. Yoshida, N. ^{15}N-depleted N_2O as a product of nitrification. *Nature* **355,** 528–529 (1988).
15. Yoshinari, T. & Wahlen, M. Oxygen isotope ratios in N_2O from nitrification at a wastewater treatment facility. *Nature* **317,** 349–350 (1985).
16. Li, Y.-H., Peng, T.-H., Broecker, W. S. & Östlund, H. G. The average vertical mixing coefficient for the oceanic thermocline. *Tellus B* **36,** 212–217 (1984).
17. Jørgensen, B. B. A theoretical model of the stable sulfur isotope distribution in marine sediments. *Geochim. Cosmochim. Acta* **43,** 363–374 (1979).
18. Nevison, C. D., Weiss, R. F. & Erickson, D. J. Global oceanic emissions of nitrous oxide. *J. Geophys. Res.* **100,** 15809–15820 (1995).
19. Rahn, T. & Wahlen, M. Stable isotope enrichment in stratospheric nitrous oxide. *Science* **278,** 1776–1778 (1997).
20. Codispoti, L. A. & Christiansen, J. P. Nitrification, denitrification and nitrous oxide cycling in the eastern tropical South Pacific Ocean. *Mar. Chem.* **16,** 277–300 (1985).
21. Law, C. S. & Owens, N. J. P. Significant flux of atmospheric nitrous oxide from the northwest Indian Ocean. *Nature* **346,** 826–828 (1990).
22. Naqvi, S. W. A. & Noronha, R. J. Nitrous oxide in the Arabian Sea. *Deep-Sea Res.* **38,** 871–890 (1991).
23. Yoshinari, T. *et al.* Nitrogen and oxygen isotopic composition of N_2O from suboxic waters of the eastern tropical North Pacific and the Arabian Sea—measurement by continuous-flow isotope-ratio monitoring. *Mar. Chem.* **56,** 253–264 (1997).
24. Naqvi, S. W. A. *et al.* Budgetary and biogeochemical implications of N_2O isotope signatures in the Arabian Sea. *Nature* **394,** 462–464 (1998).
25. Cline, J. D., Wisegarver, D. P. & Kelly-Hansen, K. Nitrous oxide and vertical mixing in the equatorial Pacific during the 1982–1983 El Niño. *Deep-Sea Res.* **34,** 857–873 (1987).
26. Karl, D. M. *et al.* Ecosystem changes in the North Pacific subtropical gyre attributed to the 1991–92 El Niño. *Nature* **373,** 230–234 (1995).
27. Sansone, F. J., Popp, B. N. & Rust, T. M. Stable carbon isotopic analysis of low-level methane in water and gas. *Anal. Chem.* **69,** 40–44 (1997).
28. Popp, B. N., Sansone, F. J., Rust, T. M. & Merritt, D. A. Determination of concentration and carbon isotopic composition of dissolved methane in sediments and nearshore waters. *Anal. Chem.* **67,** 405–411 (1995).
29. Craig, H. Isotopic standards for carbon and oxygen and correction factors for mass-spectrometric analysis of carbon dioxide. *Geochim. Cosmochim. Acta* **12,** 133–149 (1957).
30. Brand, W. A. PRECON: a fully automated interface for the pre-GC concentration of trace gases in air for isotopic analyses. *Isotopes Environ. Health Stud.* **31,** 277–284 (1995).
31. Yoshida, N. & Matsuo, S. Nitrogen isotope ratio of atmospheric N_2O as a key to the global cycle of N_2O. *Geochem. J.* **17,** 231–239 (1983).

Acknowledgements. We thank the members of the Hawaii Ocean Time-series (HOT) program and M. E. Holmes for sample collection, and T. Rust for technical support. This research was supported by the US National Science Foundation.

Correspondence and requests for materials should be addressed to J.D. (e-mail: asjdore@ilhawaii.net). Supporting data sets from station ALOHA are available at http://hahana.soest.hawaii.edu.

Dating topography of the Sierra Nevada, California, using apatite (U–Th)/He ages

Martha A. House*†, Brian P. Wernicke* & Kenneth A. Farley*

** Division of Geological and Planetary Sciences, California Institute of Technology, Pasadena, California 91125, USA*

The upward motion of rock masses relative to the Earth's surface has been documented for most of the main mountain belts using thermochronological and petrological techniques. More fundamental to the physical processes of mountain building, however, is the motion of the Earth's surface itself, which remains elusive[1]. Here we describe a technique for estimating the age of topographic relief by mapping the low-temperature thermal structure imparted by river incision using the ages of apatites determined from their uranium, thorium and helium contents. The technique exploits horizontal variations in temperature in the shallow crust that result from range-normal river drainages[2,3], because cooling beneath ancient river valleys occurs earlier than beneath intervening ridges. Our results from the Sierra Nevada, California, indicate that two of the modern transverse drainages, the Kings and the San Joaquin, had developed deep canyons by the Late Cretaceous period, suggesting that the high topography of the range is ~50–60 million years older than generally thought[4–6].

Neglecting lateral variations in reduced heat flux, radioactive heat production, mean surface temperature and advection of heat due to erosion, the temperature T in the shallow crust below a periodic topography is given by:

$$T = T_0 + \frac{q_m z}{k} + \frac{\rho H_s h_r^2}{k}(1 - e^{-z/h_r}) + \left(\beta - \frac{q_m}{k} - \frac{\rho H_s h_r}{k}\right) h_0 \cos\frac{2\pi x}{\lambda} e^{-2\pi z/\lambda} \quad (1)$$

where x and z are horizontal distance and depth below mean elevation, respectively, h_0 and λ are amplitude and wavelength of relief, respectively[7], ρH_s and q_m are surface radioactive heat production and reduced heat flow, respectively, and the remaining variables are described in Fig. 1 legend. For a mountain belt with a geothermal gradient near 20 °C km^{-1}, lapse rate of surface temperature β of 4.5 °C km^{-1} (ref. 8), and relief $2h_0$ of 2 km, the maximum horizontal variation in temperature near $z = h$ is ~30 °C. Because the thermal amplitude attenuates with characteristic depth $\lambda/2\pi$, cooling ages would be most sensitive to long-wavelength topography in the upper few kilometres of the crust.

The thermochronometer with the greatest potential for measuring this effect is the (U–Th)/He method on apatite[9], which has a closure temperature near 75 °C (ref. 10). For this system, we wish to know what horizontal age variation, Δt, results from a given h_0 and

† Present address: Department of Earth & Atmospheric Sciences, Saint Louis University, St. Louis, Missouri 63103, USA.

λ, the two parameters that define the topography. For a thermal and erosional history relevant to the Sierra Nevada (Fig. 1), we obtain $\Delta t \sim 20$ Myr, using equation (1) and a numerical solution to the He production-diffusion equation[11] (using experimentally derived diffusion parameters for He in apatite[10]). Because uncertainties in (U–Th)/He ages are typically <5% (or <5 Myr for samples with Cretaceous/Tertiary ages), age variations due to topography should be detectable. Age variation is strongly dependent on h_0 (Δt ranging from 3 to 40 Myr for canyons 0.4–6.0 km deep), and less sensitive to λ (Δt ranging from 20 to 27 Myr for wavelength of 20–70 km). Therefore, horizontal age profiles should constrain the palaeotopography, wherein observed periodicity in age would yield λ, the oldest ages would yield a minimum age for river incision, and Δt would be used to estimate h_0, provided that the geotherm and cooling history could be estimated.

Several important effects would damp thermal topography, leading to an underestimate of relief $2h_0$ for a given age contrast

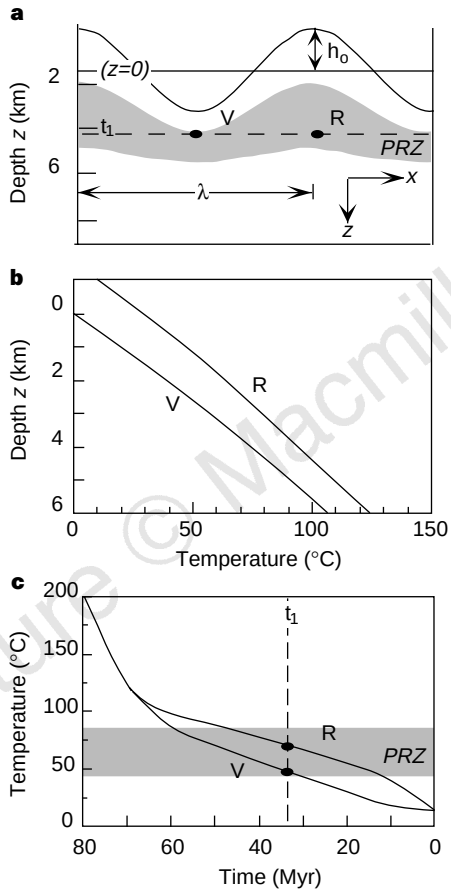

Figure 1 Thermal history of rock samples below periodic topography. **a**, Schematic range-parallel cross-section showing the influence of topography on isotherms bounding the partial retention zone (PRZ, shaded) for helium in apatite (45–85 °C; ref. 11). At time t_1, the sample below the valley (V) is nearly closed to helium diffusion, while the sample below the ridge (R) remains open, resulting in a younger (U–Th)/He age beneath the ridge. **b**, Steady-state geotherms beneath valley and ridge sites described by equation (1) using nominal central Sierran heat-flow parameters[13] of reduced heat flow q_m (21 mW m^{-1}), characteristic depth of heat production h_r (10 km), thermal conductivity k (2.4 W K^{-1} m^{-1}), surface radioactive heat production ρH_s (1 μW m^{-3}), temperature at depth $z = 0$ km T_o (15 °C), and lapse rate of mean surface temperature β (4.5 °C km^{-1}). **c**, Hypothetical cooling histories of valley and ridge samples. Rapid cooling trajectory above ~100 °C based on higher temperature thermochronometers for central Sierra[15,16]. Trajectory through PRZ assumes unroofing at a constant rate of 0.08 mm yr^{-1} of a steady-state topography with $h_0 = 1$ km and $\lambda = 70$ km from a depth $z = 6$ km at 80 Myr, using geotherms from **b**.

Δt. One is advection, which is not likely to be important in the slowly eroding Sierra Nevada, but could be important in other mountain belts. A second is cooling from the eastern or western edges of the Sierra Nevada proper, where incision would be near zero and isotherms more planar. A third includes groundwater flow, wherein a regional aquifer transports heat from high areas to low areas[12].

To test the technique, we collected 36 samples for (U–Th)/He dating along a 200-km range-parallel transect through the southern Sierra Nevada batholith, crossing the points of maximum valley incision at elevations near 2 km (Fig. 2). We chose the Sierra Nevada because it is a relatively simple west-tilted block. Its western margin has been near sea level since at least 80 Myr ago[4,5] and there is no evidence of significant folding or faulting along the transect, or within the Great Valley sedimentary prism to the west. The heat production of Sierran plutons, which if strongly variable along the transect would compromise the technique, varies mainly in a direction normal to the range axis[13]. To obtain a nearly horizontal profile, samples near the modern valleys were collected from local summits and those from intervening ridges were collected from the bottoms of secondary valleys. To avoid any effects from local, small-volume Late Cenozoic igneous centres, we did not sample from within a few kilometres of them. Samples were taken from below the upper 10 cm of the bedrock surface to avoid transient thermal effects including lightning, forest fires and afternoon heating[11].

Total erosion of this part of the range since the end of granitic plutonism at 80–85 Myr ago is ~6–8 km (ref. 14), yielding an average erosion rate of ~0.10 mm yr^{-1}. This rate is broadly consistent with the incision rate of the San Joaquin River since the deposition (~10 Myr ago) of fluvial gravels along the western flank of the range[10], which extend eastwards to within 10 km of our sample traverse[4], and with unroofing rates estimated from the tilt history of Cenozoic sediments in the Great Valley[5]. Age–elevation profiles from the Kings and Merced drainages based on apatite and sphene fission-track data indicate rapid cooling from 270 to 100 °C from 75 to 65 Myr ago[15]. In contrast, (U–Th)/He ages from the same apatite separates yielded ages ranging from 30 to 75 Myr with a well defined elevation gradient of ~20 Myr km^{-1} (ref. 16). These data, combined with modern heat-flow measurements, indicate low to moderate geothermal gradients (10–25 °C km^{-1}) in the uppermost crust since ~70 Myr ago[13,15,16].

When projected onto the line of section in Fig. 2, the age profile is periodic with $\lambda \approx 70$ km and $\Delta t \approx 20$–30 Myr, crudely mirroring

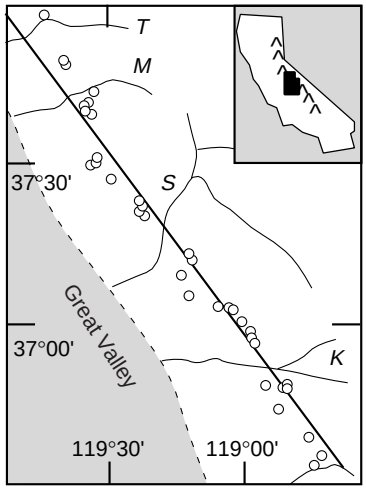

Figure 2 Study area. Shown are sample locations (open circles) and position of topographic profile (heavy line) in the Sierra Nevada, spanning the Tuolumne (T), Merced (M), San Joaquin (S) and Kings (K) drainages. The boundary between San Joaquin Valley (grey) and Sierra Nevada is indicated by the dashed line. Inset, location of Sierran crest (inverted 'vee' symbols) in the state of California.

the modern topography (Fig. 3). The widths of the age peaks appear to correlate with the widths of the valleys, with a wider peak for the San Joaquin drainage than for the Kings, and no apparent age effect for the much smaller Merced and Tuolumne drainages. The age profile, if indeed the result of palaeotopography, suggests that the large canyons of the San Joaquin and Kings rivers were incised by 70–80 Myr ago, whereas the smaller Tuolumne and Merced drainages were either too small to have a thermal effect or had not yet been formed. Other explanations for the variation, including heat production contrasts, Late Cenozoic magmatism, or kilometre-scale folding or faulting normal to the range axis, are inconsistent with the structural and thermal history of the range, as discussed above.

According to our calculations relating age variations to topographic amplitude in the Sierras, the observed 20–30 Myr variation in helium ages correspond to long-wavelength relief of 2–4 km. A more precise estimate will be possible using more detailed numerical calculations and sensitivity analysis of the function $h_0(\Delta t)$ to various assumptions regarding the geotherm and unroofing history (M.A.H. *et al.*, manuscript in preparation). Whatever the precise estimate, it represents a minimum for the Late Cretaceous mean elevation at the crest of the range. First, by analogy with the modern high ranges, we expect the amplitude of short-wavelength topography ($\lambda < 20$ km) to have been at least 250 m (Fig. 3b), adding about 500 m to the total relief. Second, the crests of mountain ranges are substantially higher than ridge elevations where relief is maximum. For example, the crest of the modern Sierra lies 45 km northeast of our profile, with both mean and summit elevations ~30% higher than those along the profile. If we incorporate these factors into a Cretaceous elevation model with long-wavelength relief of 3 km (corresponding to Δt of 25 Myr), we infer mean elevation of the Sierran crest of ~4.5 km, a value similar to that of the modern central Andes.

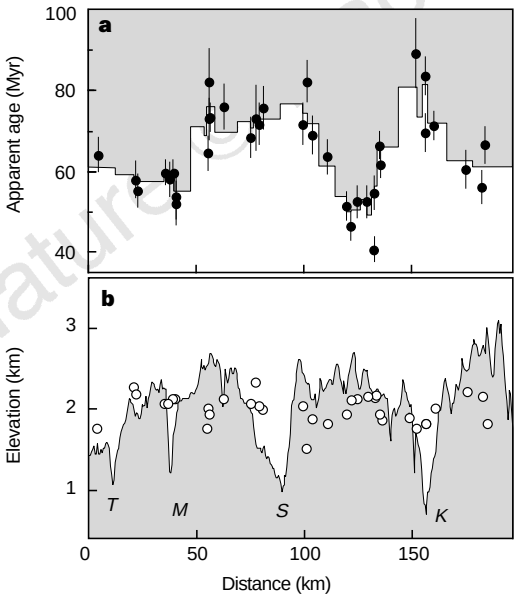

Figure 3 (U–Th)/He ages along range-parallel profile. **a**, Elevation-adjusted helium ages for samples projected onto profile in Fig. 2. Helium and U–Th analyses were performed on the same aliquots at Caltech following procedures in refs 16, 26. Samples of euhedral, inclusion-free igneous apatite from undeformed granitic plutons were analysed in replicate, with mean ages ranging from 44.5 to 84.6 Myr. Errors shown are 1σ and reflect analytical uncertainties in helium and U–Th measurements[16,26]. Ages were corrected for small differences in sample elevation above or below 2,000 m using the observed age–elevation gradient[16]. Stepped curve is defined by three-sample average of elevation-adjusted ages. A complete table of analytical results is available; see Supplementary Information. **b**, Location and elevation of samples projected onto profile in Fig. 2, plotted with topography along profile. Drainages are labelled as in Fig. 2.

Cretaceous relief may be estimated independently of Δt by considering the difference between erosion of the valleys after initial incision and the total erosion since the Cretaceous. To preserve their old ages, the valley samples must have cooled below 50 °C by 70–80 Myr ago, implying 2–4 km of valley erosion above the 2,000-m profile since that time (assuming a geothermal gradient of 10–25 °C km^{-1}, ref. 16, Fig. 3b). Provided that total erosion of the central Sierra since 80 Myr ago was 6–8 km, and the ridges were eroding at a nominal rate of ~0.1 mm yr^{-1} during the late Cretaceous (1 km of erosion between 70 and 80 Myr ago), then the ridges would have stood ~3 km above the valleys at ~70 Myr ago, similar to the estimate based on the age variations.

The modern relief is ~1 km along the profile (Fig. 3b) and the mean elevation of the crest of the range is[17] 2.8 km, implying that (1) the average erosion rate of the ridges was roughly twice that of the valleys since ~70 Myr ago, leading to an overall reduction in Cenozoic relief, and (2) that mean elevation has decreased since 70 Myr ago. A model of decreasing mean elevation and relief since the Cretaceous challenges the long-standing hypothesis, based on palaeobotanical and geomorphological arguments, that the Sierra were a low-standing range of subdued relief for most of early Tertiary time, followed by rapid uplift to its current mean crestal elevation in the past 10–20 Myr (refs 4, 6). However, reinterpretation of the geomorphic data in terms of a flexural-isostatic uplift model is consistent with progressive lowering of mean elevation since the Cretaceous[18], and the profound buoyancy loss of the crust since 20 Myr ago due to crustal thinning poses difficulties[19]. Further, the basis of the earlier palaeobotanical interpretations is in dispute[20], and recent work on floras in western Nevada, previously thought to indicate uplift over the past 10 million years, suggest a loss of some 1.5 km in mean elevation between 16 Myr ago and the present[21].

If our inferences regarding Late Cretaceous relief are to be reconciled with a low-elevation, low-relief Sierra in the early Tertiary, it would require reduction of mean elevation of ~2 km in just 10–20 million years. Such a reduction could not be purely erosional, because isostatic considerations require at least 10–15 km of erosion, more than double the total post-85-Myr erosion. The only likely tectonic explanation for a significant post-batholithic, pre-extensional buoyancy loss would be the generation of the thick column of upper-mantle eclogitic rocks known from xenolith studies[22] at the base of the cooling Sierran batholith. However, the age of crystallization of the eclogitic rocks is 80–120 Myr (ref. 23), too early to account for significant post-batholithic lowering[23].

We conclude that the Sierra developed an Andean-scale topography between ~185 Myr (the youngest marine strata preserved in batholith wallrocks[24]) and 70–80 Myr (the minimum age of deep incision), coinciding with crustal thickening via arc magmatism in the Sierra and contractional deformation to the east. By 70–80 Myr ago, both the San Joaquin and Kings drainages had deeply incised the western flank of the range, after which we infer gradual reduction of mean crestal elevation from ~4.5 km to 2.8 km and of long-wavelength relief from ~3 km to 1 km. Although the buoyancy loss from crustal thinning since 20 Myr would presumably have resulted in accelerated loss of mean elevation, the synchronous loss of a cold, eclogitic root and its replacement with hot peridotite, especially near the crest of the range[19,22,25], may have added comparable or greater buoyancy. So it remains an open question whether these tectonic influences on buoyancy augmented or diminished the loss of mean elevation due to erosion since 20 Myr ago (ref. 18). □

Received 10 December 1997; accepted 27 July 1998.

1. England, P. C. & Molnar, P. Surface uplift, uplift of rocks and exhumation of rocks. *Geology* **18,** 1173–1177 (1990).
2. Mancktelow, N. S. & Grasemann, B. Time-dependent effects of heat advection and topography on cooling histories during erosion. *Tectonophysics* **270,** 167–195 (1997).

3. Stüwe, K., White, L. & Brown, R. The influence of eroding topography on steady-state geotherms. Application to fission track analysis. *Earth Planet. Sci. Lett.* **124,** 63–74 (1994).
4. Huber, N. K. Amount and timing of late Cenozoic uplift and tilt of the central Sierra Nevada, California—Evidence from the upper San Joaquin River basin. *US Geol. Surv. Prof. Pap.* **1197,** 1–28 (1981).
5. Unruh, J. R. The uplift of the Sierra Nevada and implications for late Cenozoic epeirogeny in the western Cordillera. *Geol. Soc. Am. Bull.* **103,** 1395–1404 (1991).
6. Axelrod, D. I. in *Integrated Earth and Environmental Evolution of the Southwestern U.S.* (eds Ernst, W. G. & Nelson, C. A.) 70–79 (Bellweather, Columbia, MD, 1998).
7. Turcotte, D. L. & Schubert, G. *Geodynamics* (Wiley, New York, 1982).
8. Birch, F. Flow of heat in the Front Range, Colorado. *Geol. Soc. Am. Bull.* **61,** 567–630 (1950).
9. Zeitler, P. K., Herczig, A. L., McDougall, I. & Honda, M. U-Th-He dating of apatite: a potential thermochronometer. *Geochim. Cosmochim. Acta* **51,** 2865–2868 (1987).
10. Wolf, R. A., Farley, K. A. & Silver, L. T. Helium diffusion and low temperature thermochronometry of apatite. *Geochim. Cosmochim. Acta* **60,** 4231–4240 (1996).
11. Wolf, R. A., Farley, K. A. & Kass, D. M. Modeling of the temperature sensitivity of the apatite (U-Th)/He thermochronometer. *Chem. Geol.* **148,** 105–114 (1998).
12. Lachenbruch, A. H. & Sass, J. H. in *The Earth's Crust; Its Nature and Physical Properties* (eds Heacock, J. G. *et al.*) 626–675 (Am. Geophys. Union, Washington DC, 1977).
13. Saltus, R. W. & Lachenbruch, A. H. Thermal evolution of the Sierra Nevada: implications of new heat flow data. *Tectonics* **10,** 325–344 (1991).
14. Ague, J. J. & Brimhall, G. H. Magmatic arc asymmetry and distribution of anomalous plutonic belts in the batholiths of California: Effects of assimilation, crustal thickness, and depth of crystallization. *Geol. Soc. Am. Bull.* **100,** 912–927 (1988).
15. Dumitru, T. A. Subnormal Cenozoic geothermal gradients in the extinct Sierra Nevada magmatic arc: consequences of Laramide and post-Laramide shallow-angle subduction. *J. Geophys. Res.* **95,** 4925–4941 (1990).
16. House, M. A., Wernicke, B. P., Farley, K. A. & Dumitru, T. A. Cenozoic thermal evolution of the central Sierra Nevada, CA from (U-Th)/He thermochronometry. *Earth Planet. Sci. Lett.* **151,** 167–179 (1997).
17. Diment, W. H. & Urban, T. C. Average elevation map of the conterminous United States (Gilluly averaging method). *US Geol. Surv. Geophys. Invest. Map* **933,** (1981).
18. Small, E. E. & Anderson, R. S. Geomorphically driven Late Cenozoic rock uplift in the Sierra Nevada, California. *Science* **270,** 277–280 (1995).
19. Wernicke, B. *et al.* Origin of high mountains in the continents: the southern Sierra Nevada. *Science* **271,** 190–193 (1996).
20. Wolfe, J. A. An analysis of present-day terrestrial lapse rates in western conterminous United States and their significance to paleoaltitudinal estimates. *US Geol. Surv. Bull.* **1964,** 35 (1992).
21. Wolfe, J. A., Schorn, H. E., Forest, C. E. & Molnar, P. Paleobotanical evidence for high altitudes in Nevada during the Miocene. *Science* **276,** 1672–1675 (1997).
22. Ducea, M. N. & Saleeby, J. B. Buoyancy sources for a large, unrooted mountain range, the Sierra Nevada, California: Evidence from xenolith thermobarometry. *J. Geophys. Res.* **101,** 8229–8244 (1996).
23. Ducea, M. N. & Saleeby, J. B. The age and origin of a thick mafic-ultramafic root from beneath the Sierra Nevada batholith: Part I: Geochronology. *Contrib. Mineral. Petrol.* (in the press).
24. Saleeby, J. B. & Busby-Spera, C. in *The Cordilleran Orogen: Conterminous U.S.* (eds Burchfiel, B. C., Lipman, P. W. & Zoback, M. L.) 107–168 (Geol. Soc. Am. DNAG G3, Boulder, 1992).
25. Park, S. K., Hirasuna, B., Jiracek, G. R. & Kinn, C. Magnetotelluric evidence of lithospheric mantle thinning beneath the southern Sierra Nevada. *J. Geophys. Res.* **101,** 16241–16255 (1996).
26. Farley, K. A., Wolf, R. A. & Silver, L. T. The effects of long alpha-stopping distances on (U-Th)/He dates. *Geochim. Cosmochim. Acta* **60,** 4223–4230 (1996).

Supplementary information is available on *Nature*'s World-Wide Web site (http://www.nature.com) or as paper copy from the London editorial office of *Nature*.

Acknowledgements. This work is part of the Southern Sierra Nevada Continental Dynamics Project, supported by NSF's Continental Dynamics Program. We thank M. Ducea and J. Saleeby for permission to discuss their results before publication.

Correspondence and requests for materials should be addressed to M.A.H. (e-mail: house@eas.slu.edu).

Mycorrhizal fungal diversity determines plant biodiversity, ecosystem variability and productivity

Marcel G. A. van der Heijden*†, John N. Klironomos†‡, Margot Ursic‡, Peter Moutoglis§, Ruth Streitwolf-Engel*, Thomas Boller*, Andres Wiemken* & Ian R. Sanders*

** Botanisches Institut der Universität Basel, Hebelstrasse 1, 4056 Basel, Switzerland*
‡ Department of Botany, University of Guelph, Ontario N1G 2W1, Canada
§ Premier Tech Riviere-du-Loup, Quebec G5R 4C9, Canada
† These authors contributed equally to this work

The functioning and stability of terrestrial ecosystems are determined by plant biodiversity and species composition[1–5]. However, the ecological mechanisms by which plant biodiversity and species composition are regulated and maintained are not well understood. These mechanisms need to be identified to ensure successful management for conservation and restoration of diverse natural ecosystems. Here we show, by using two independent, but complementary, ecological experiments, that belowground diversity of arbuscular mycorrhizal fungi (AMF) is a major factor contributing to the maintenance of plant biodiversity and to ecosystem functioning. At low AMF diversity, the plant species composition and overall structure of microcosms that simulate European calcareous grassland fluctuate greatly when the AMF taxa that are present are changed. Plant biodiversity, nutrient capture and productivity in macrocosms that simulate North American old-fields increase significantly with increasing AMF-species richness. These results emphasize the need to protect AMF and to consider these fungi in future management practices in order to maintain diverse ecosystems. Our results also show that microbial interactions can drive ecosystem functions such as plant biodiversity, productivity and variability.

The mechanisms that control plant biodiversity are still being debated. The ability of many plant species to co-exist, and thus to determine plant biodiversity, can be explained by competitive interactions[6,7], by spatial or temporal resource partitioning[8,9], by disturbance creating new patches for colonization[10,11], and by interactions among different functional groups of organisms that constitute ecosystems[12–15]. So far, little attention has been paid to the effects of microbe–plant interactions, particularly the mycorrhizal symbiosis, on ecosystem variability, productivity and plant biodiversity. AMF are abundant in soils of most ecosystems; these fungi form mutualistic symbiotic associations with the roots of ~80% of all terrestrial plant species, thereby acting as extensions of plant root systems and increasing nutrient uptake, especially of phosphorus[16]. The presence of AMF in ecosystems increases plant biodiversity[17]. However, not only are AMF present in most ecosystems, but communities of AMF also occur, which vary in species composition, species number and, therefore, in AMF biodiversity[18,19]. Furthermore, AMF biodiversity is greatly reduced in some ecosystems[20]. Different AMF species induce differential growth responses, in terms of biomass production and clonal growth patterns, of coexisting plant species of calcareous grasslands[21,22]. On the basis of these results, we proposed that the species composition and diversity of AMF communities have the potential to determine plant biodiversity in natural ecosystems[22].

Here we show for the first time, to our knowledge, that species composition and species richness of AMF is an important contributor to plant species composition, variability, productivity and biodiversity in artificial microcosms and macrocosms.

In a greenhouse experiment (experiment 1), we compared the effects of four different native AMF taxa, which were all isolated from the soil of a calcareous grassland, and of a combination of these four AMF taxa on the species composition and structure of 48 microcosms simulating European calcareous grassland. When we compared any of these AMF treatments with the non-mycorrhizal control treatment, we found that eight of the eleven plant species were almost completely dependent on the presence of AMF to be successful in the microcosms (Fig. 1; plant species: *Brachypodium pinnatum*, *Centaurium erythrea*, *Hieracium pilosella*, *Lotus corniculatus*, *Prunella grandiflora*, *Prunella vulgaris*, *Sanguisorba officinalis* and *Trifolium pratense*). In contrast, *Carex flacca*, the only plant species of the microcosms that does not have a symbiotic relationship with AMF, had the highest biomass in the non-mycorrhizal treatment (Fig. 1f). Furthermore, the biomass produced by most of the plant species varied significantly among treatments with different single AMF taxa (Fig. 1), indicating that different plant species benefited to different extents from different AMF taxa. For example, the biomass of *Sanguisorba officinalis* and of *Trifolium pratense* was highest in microcosms inoculated with AMF A; the biomass of *Brachypodium pinnatum* was highest in microcosms containing AMF C; the biomass of *Prunella vulgaris* was highest in microcosms containing AMF D (Fig. 1e, h–j). Although altering the AMF taxa in the soil had no significant effect on the biomass of